Chapter 1
Laser-Induced Bubble Generation on Excitation of Gold Nanoparticles

Shuichi Hashimoto and Takayuki Uwada

Abstract This chapter focuses on pulsed-laser-induced explosive boiling of the liquid medium adjacent to gold nanoparticles that are suspended in solution. Although the laser-induced cavitation via multiphoton absorption has been known for a long time, photothermal generation of steam bubbles on irradiating the nanoparticles is by far efficient because of surface plasmon excitation. Basic properties of pulsed-laser-induced photothermal bubbles such as threshold laser fluences, bubble lifetimes and nanoparticle temperatures have been investigated experimentally. Such experiments inspired much interest from theoretical and computational studies, which accelerated thorough understanding of the fundamental processes of the temperature-induced phase transition confined to the local area surrounding the nanoparticles. Furthermore, it has been demonstrated recently that photothermal bubbles have found unprecedented applications such as promoting microscale lasing, enormously enhancing the speed of photophoretic movement for nanoparticles and sensitizing photoporation through cell membranes. We will discuss the application point of view also in this task. Finally, we will refer to underlying challenges and future prospects of the transient vapor nanobubbles.

Keywords Gold nanoparticles · Pulsed-laser excitation · Localized surface plasmon resonance · Plasmonic nanobubbles · Photothermal effect

1.1 Introduction

Gold nanoparticles (Au NPs) that represent plasmonic nanoparticles are excellent light absorbers and light scatterers at the resonance wavelengths in the visible region.

S. Hashimoto (✉)
Advanced Engineering Courses, NIT Gunma College, 580 Toriba-machi, Maebashi 371-8530, Japan
e-mail: hashichem@gunma-ct.ac.jp

T. Uwada
Department of Chemistry, Josai University, 1 Chome-1 Keyakidai, Sakado, Saitama 350-0248, Japan
e-mail: uwada@josai.ac.jp

Y. Ishikawa et al. (eds.), *High-Energy Chemistry and Processing in Liquids*,
https://doi.org/10.1007/978-981-16-7798-4_1

512121_1_En_1_Chapter ☑ TYPESET ☐ DISK ☐ LE ☑ CP Disp.:27/12/2021 Pages: 20 Layout: T1-Standard

This is because Au NPs greater than 2–3 nm support localized surface plasmon resonance (LSPR) that is described by a coherent oscillation of conduction-band electrons interacting with incoming light [1]. The excitation of LSPR affords an ultrafast series of events [2]. Photoexcitation of AuNPs and subsequent relaxation processes are given briefly in Fig. 1.1. Figure 1.1a represents LSPRs or simply plasmons, and this LSPR collects incident light far more efficiently than the physical cross section of the Au NP (Fig. 1.1a lower column). LSPRs have incredibly short lifetime and decay both radiatively and nonradiatively (Fig. 1.1b). The former plays a key role in the plasmonic enhancement of the electric field in the near-field regime, whereas the latter decay is responsible for generating hot electrons of very high kinetic energies (Fig. 1.1b lower column). The hot electrons decay through collisions with electrons and lattice (Fig. 1.1c): relaxation from a non-Fermi to Fermi electron distribution through electron–electron (e–e) scattering, cooling of hot-electron gas through electron–phonon (e–ph) scattering and heat dissipation from Au NPs to the environment (Fig. 1.1d) through phonon–phonon (ph–ph) scattering.

This chapter focuses on interaction of pulsed lasers with plasmonic nanoparticles suspended in solution, resulting in vapor nanobubble generation. As mentioned above, thermal conduction from photo-irradiated NPs raises the temperature of the surrounding medium (Fig. 1.1d). When the medium heating exceeded the threshold of liquid–gas phase transition, bubbles were generated through boiling of the local liquid next to the NPs, while liquid bath is at room temperature [3, 4]. In this context, such vapor nanobubbles are photothermally generated nanobubbles because light-to-heat conversion by Au NP is the fundamental origin. The photothermal nanobubbles

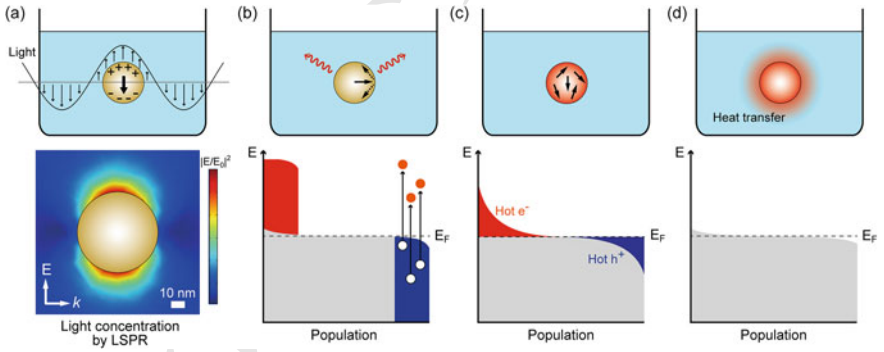

Fig. 1.1 Sequential events that occur on photoexcitation of AuNPs. **a** upper: light absorption generates LSPR that is a coherent oscillation of conduction electrons. Lower: light condensation that is significantly greater than its physical cross section. **b** In the first 1–100 fs following Landau damping, the non-thermal distribution of electron–hole pairs decays either through re-emission of photons or through carrier multiplication caused by electron–electron interactions. **c** Hot carriers will redistribute their energy by electron–electron scattering processes on a timescale ranging from 100 fs to 1 ps. **d** Heat conduction to the surroundings on a timescale ranging from 100 ps to 10 ns. E_F represents Fermi energy

are transient species and have a typical lifetime of a few nanoseconds when the duration of laser pulses used for generation is shorter than 10 ns. The bubble formation occurred in water from a superheated liquid state at approximately 550 K, not at the boiling temperature of 373 K [5]. This phenomenon may deserve commenting, and we will come back this point later. The bubble lifetimes were largely dependent on the maximum bubble sizes. Further, the threshold laser fluence, the onset of nanobubble production, depended on the NP diameter [6–8]. The detailed discussion of the bubble threshold may shed light on the fundamental process of heat transfer leading to bubble formation [9, 10]. Here, we highlight the photothermal micro/nanobubbles that dynamically grow and collapse on the surface of NPs subject to short pulsed-laser illumination. Note that the discussion of cavitation bubbles is not within the scope of our study because the cavitation bubbles have been observed on pulsed-laser illumination of liquids in the absence of NPs [11]. Cavitation is a phenomenon in which the static pressure of a liquid reduces to below the liquid's vapor pressure, leading to the formation of small vapor-filled cavities in the liquid.

This chapter will not include the description of bubble formation through continuous wave (CW) laser illumination of Au NPs because of a limited space. Due to long lifetimes up to several seconds, the CW laser-induced bubbles provided rich physics and chemistry [12]. Readers interested in further information are encouraged to refer to the literature [13]. At this moment, we should point out the merit of transient nanobubbles generated by short pulse excitation over the long-lived bubbles produced by CW illumination. By outputting a high peak power within a limited pulse duration, pulsed-laser excitation can provide the means to obtain high spaciotemporal control for bubbles. Since the heat transfer to the medium completes within nano- to microseconds, medium heating is insignificant without heat accumulation. As a result, bubble energy can effectively be applied for mechanical works and shock/acoustic waves. On the other hand, CW laser excitation results in significant heat accumulation that can be inadequate for biological systems.

1.2 Bubble Generation on Short Pulsed-Laser Excitation of Colloidal Au NPs

Historically speaking, photothermal microbubbles have been observed by diffraction-limited imaging on pulsed-laser irradiation of black microparticles suspended in solution [14]. Subsequently, the Plech group pursued picosecond time-resolved studies of nanobubble dynamics on femtosecond laser excitation of colloidal Au NPs, combined with monitoring by the picosecond puled X-ray scattering form a synchrotron radiation [3, 4]. The X-ray scattering was not very straightforward to visualize bubble dynamics such as diameter change with time. However, it was powerful to observe the lattice melting of Au NPs on laser illumination [15]. Thus, Au NPs were found to be heated possibly at least to a liquid state during the bubble formation. Lapotko, on the other hand, has focused on the single particle measurement of bubbles using a Au NP

immobilized on a substrate under the optical microscope [16]. Besides imaging, his group measured the time growth and decay of the light scattering signals associated with a bubble from a Au NP at a fixed wavelength on 0.5 ns pulsed-laser excitation. It was not until the picosecond time-resolved measurement by the Hashimoto group that optical extinction (absorption and scattering) spectra in the visible region were characterized for colloidal Au NPs during the bubble formation/collapse [8]. Bubble dynamics were characterized by the time-dependent spectral changes that provided the direct information of bubbles distinct from the particle heating and cooling. The three groups: Plech, Lapotko and Hashimoto have investigated experimentally the fundamental properties of plasmonic nanobubbles such as bubble nucleation temperature, threshold fluences and bubble lifetimes by taking advantage of their own methods. We will discuss below these fundamental issues regarding plasmonic nanobubbles.

Before getting into the details of nanobubble properties, we describe how we can follow the nanobubble dynamics using the optical spectroscopy. The transient extinction spectra of colloidal Au NPs exhibited the ultrafast bleaching of the characteristic LSPR band, followed by the recovery of the bleaching signals. A prototypical example is given in Fig. 1.2a in which 60-nm-diameter Au NPs were excited by a 15 ps laser at an excitation wavelength of 355 nm [8]. The transient bleaching signals were instantaneously observed with the laser pulse followed the remarkably fast recovery. The origin of such bleaching/recovery of the transient signals was ascribed to heating and cooling of the Au NPs [17]. This transient spectral change can be reproduced by LSPR spectra dependent on temperature, given in Fig. 1.2b, which is the spectral simulation based upon Mie theory [1]. With increase in temperature, LSPR undergoes the significant broadening that causes LSPR spectral bleaching in the transient spectra on laser illumination, the extent of which strongly depends on the particle temperature. It was found that the lattice temperature of ~1000 K was reached at high pump intensities. The time trace of the bleaching/recovery signals completed after a sufficient time has elapsed because of heat conduction to the surrounding medium. However, it has been demonstrated that the amplitude of the background signals increased as the pump laser intensity increased (Fig. 1.2c). The background signals are an optical signature of bubble formation. The experimental data showed a threshold laser intensity that produces the particle temperature of 550 ± 50 K [5].

The bubble signals are basically caused by Rayleigh light scattering that largely depends on the bubble diameter (r^6-dependence) [8]. A greater scattering signal is generated as the bubble diameter increases. From Fig. 1.2c, we note that the scattering from bubble is superimposed on the LSPR bleaching of Au NPs. The spectral simulation using a concentric core–shell structure of the bubble/Au NP is in Fig. 1.2d. The graph reveals that such simulated spectra well-reproduce the experimental ones and that more positive extinction signals occur for bubbles with greater diameters. Note, however, that negative extinction is predicted to occur for bubbles with small diameters in which the bubbles act to reduce the absorption of Au NP because of the reduced refractive index of the medium surrounding the Au NP, rather giving an enhanced light scattering that increases total extinction.

512121_1_En_1_Chapter ☑ TYPESET ☐ DISK ☐ LE ☑ CP Disp.:27/12/2021 Pages: 20 Layout: T1-Standard

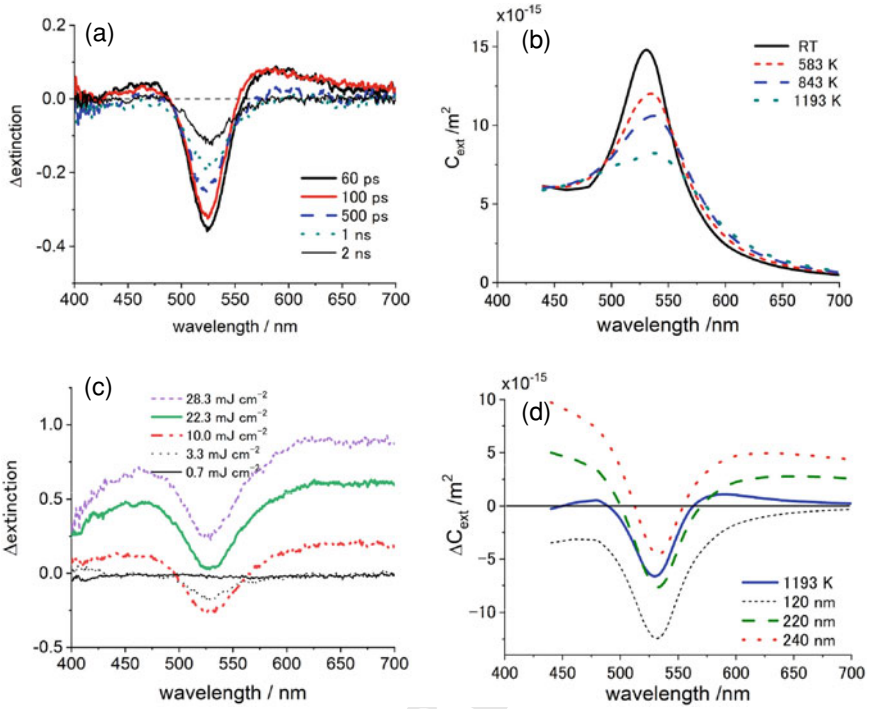

Fig. 1.2 Pump-probe measurements of transient extinction (absorption and scattering) spectra of 60-nm-diameter aqueous colloidal Au NPs excited by a 15 ps laser at the excitation wavelength of 355 nm: **a** transient extinction spectra in the absence of bubbles at 60 MPa hydrostatic pressure; **b** simulated temperature-dependent extinction spectra of 60-nm-diameter aqueous Au NP, which interpret the observation in (**a**); **c** experimental bubble spectra at various excitation intensities at a time delay of 2 ns (at 0.1 MPa); **d** simulated bubble spectra of various diameters (concentric Au NP core-bubble shell structures are assumed). Adapted with permission from Katayama et al. [8] (Copyright 2014 American Chemical Society)

We have stated already the concentric core–shell bubble model that may form because of an effective heat transfer from the metal surface. Besides the core–shell structure that was captured by optical microscopy for microbubbles, two other types have been proposed [18, 19]. Figure 1.3 summarizes the bubble models (upper) and the scanning electron microscopy (SEM) images (lower) in which bubbles were trapped using tetraethoxysilane as a trapping agent. In the SEM experiment, the bubbles were generated by irradiating nanosecond pulsed lasers with a wavelength of 355 nm in aqueous colloidal Au NPs.

In the transient X-ray scattering and extinction spectral measurements quoted above [3, 6], such a core–shell model has been successfully employed for estimating bubble diameters from time-resolved spectroscopic measurements [6, 8]. The confetti (b) can be found in the earliest stage of bubble nucleation, and this structure has been observed by the transmission electron microscopy (TEM) coupled with femtosecond

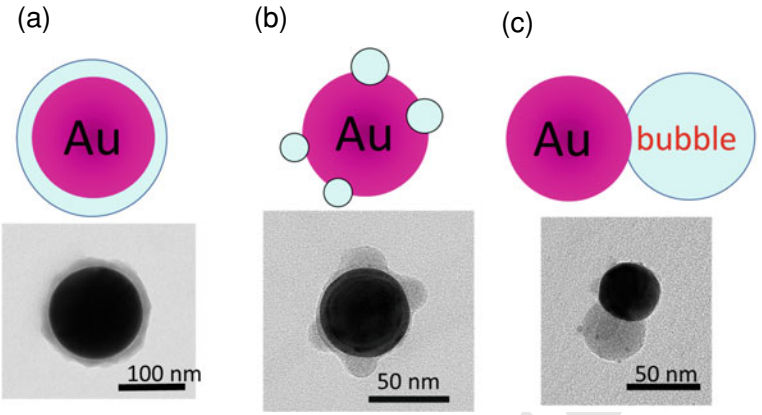

Fig. 1.3 Bubble structure models; **a** core–shell, **b** confetti and **c** Janus. SEM images are unpublished results from Hashimoto laboratory

laser excitation [18]. The Janus structure (c) has been proposed initially without experimental proof [19]. The bubble trapping experiment suggested indirectly the existence of all three structures at the nanoscale.

Now, we discuss three important properties of bubbles, bubble generation temperature (~550 K), threshold laser fluence and bubble lifetimes. First, we interpret how the pulsed-laser-induced plasmonic bubbles have been rationalized to occur from superheated solvent next to the NPs using the phase diagrams of water [20]. Figure 1.4a upper column compares line shapes of P(V) at different temperatures for Van der Waals fluid. Notably, the boiling temperature T_b and critical temperature T_c are of relevance to the phase transitions. At temperatures above T_c, the isotherms are monotonic, implying that only one state can exist at a given pressure. At temperatures below T_c, phase coexistence of liquid (L) and gas (G) can occur. Liquid-to-gas transition occurs along the line L to G. A red line shows the coexistence curve, and the light blue area represents the region of coexistence. Further, the yellow zone separated by a spinodal curve (red dashed line) predicts unusual behavior. In the latter area of the diagram, we can see that pressure increase causes volume expansion $(\partial P/\partial V)_T > 0$, meaning that the system is not stable. Another important point is that during the volume change from L to G on the isotherm curves molecules experience an energy barrier because of the concave shape of Helmholtz free energy, F, as shown in the lower column. The energy barrier we can see for the curve at T_b is the origin of superheating. Thus, fluid can remain liquid even if the boiling temperature is exceeded. However, the height of the energy barrier gradually decreases on going from T_b to T_c. As a result, boiling is more likely to occur for superheated water at temperatures $T > T_b$.

Figure 1.4b represents a diagram that expresses pressure as a function of temperature for water. If a Au NP in water is heated by laser illumination from 293 K at a constant pressure of 1 atm, the water temperature next to the NP increases along the

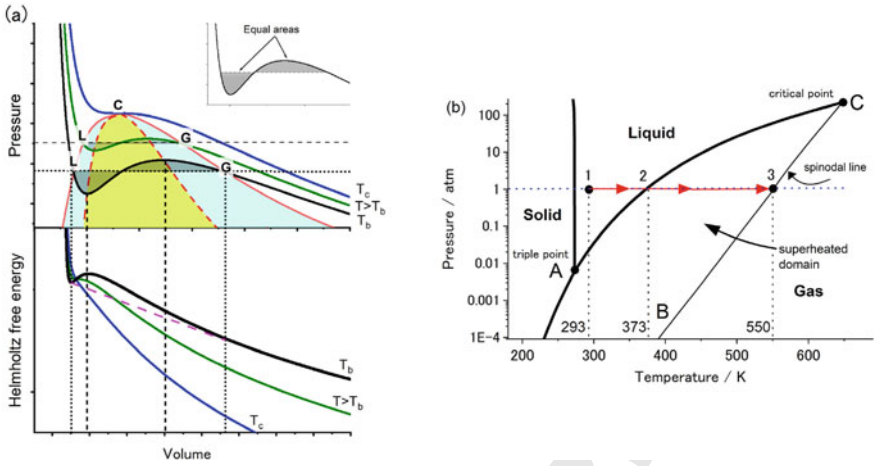

Fig. 1.4 **a** Upper: Series of P-V diagrams of isotherms of increasing temperatures from boiling temperature (T_b) to critical point (T_c); Lower: corresponding Helmholtz free energy versus V curves. **b** Phase diagram that represents pressure as a function of temperature for water. All the possible states, gas, liquid and solid, are shown

horizontal line, reaching first a boiling temperature of 373 K. If the NP is suspended in clean water contained in a chamber with smooth surfaces, it is likely that superheating occurs until the spinodal temperature of 550 K is reached. The spinodal represents the intrinsic stability limit of the liquid $\left((\partial T/\partial S)_P = 0;\ (\partial P/\partial V)_T = 0\right)$. At the spinodal, the superheated liquid phase is no longer stable with respect to the random density fluctuations [21]. As a result, an explosive boiling occurs, generating a steam bubble. This is a situation that is predicted for isolated Au NPs.

Although the heating of isolated Au NPs results in bubble generation at a particle temperature T ~ 550 K, the CW laser heating of Au NP aggregates formed in water induced formation of micrometric bubbles at a temperature that coincides with the boiling point of water under atmospheric pressure [22]. This result was interpreted by the collective heating effect [13]. If many NPs closely located are heated, water molecules undergo heating from many NPs simultaneously. As a result, the heating of the solvent is no longer limited to a nanoscale local space around a Au NP, but a certain volume of water can be heated, resulting in a situation similar to bulk heating. Further, if the CW laser is used instead of the pulse, heat accumulation takes place with time. These are the explanations for the working principle of collective heating.

Second, we look into the threshold laser fluence versus Au NP radius/diameter for bubble formation.

Figure 1.5 gives both experimental and computational curves from different laboratories.

Siems et al. observed monotonous decrease with increasing diameter (filled red squares in Fig. 1.5a) [6], whereas Katayama et al. observed a bathtub shape with a minimum at 60-nm-diameter (Fig. 1.5b) [8]. The monotonous decrease has also

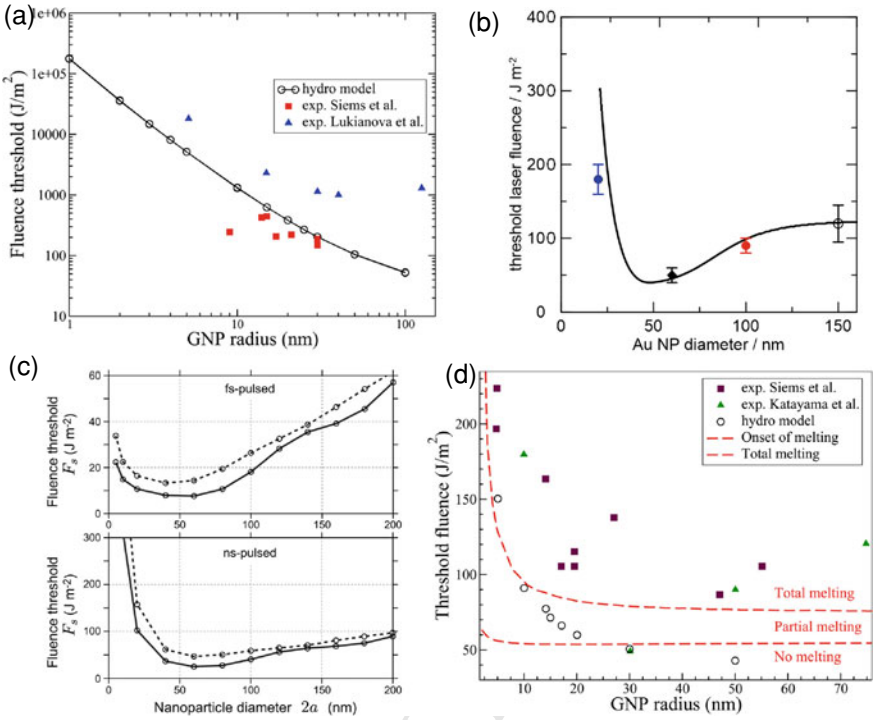

Fig. 1.5 Bubble formation threshold as a function of Au NP radius/diameter. **a** Comparison between the simulation for nanosecond pulses (Lombard et al. [10]) and the experiments by Siems et al. [6] (red squares; nanosecond pulses at the wavelength of 355 nm) and Lukianova et al. [7] (blue triangles; 0.5 ns pulses at the wavelength of 532 nm). **b** Transient extinction spectroscopy measurement with 15 ps laser excitation at a wavelength [8]. **c** Computational results by Baffou et al. [9] both for fs- and ns-pulses at the wavelengths of 355 nm (dashed line) and 532 nm (solid line). **d** Comparison between the simulation by Lombard et al. [10] and the experiments by Siems et al. [6] (red squares) and Katayama et al. [8] (blue triangles). **a** and **d** Adapted with permission from Lombard et al. [10]. (Copyright 2017 American Chemical Society). **b** Adapted with permission from Katayama et al. [8] (Copyright 2014 American Chemical Society). **c** Adapted with permission from Metwally et al. [9]. (Copyright 2015 American Chemical Society)

been observed by Lukianova et al. by using a single particle light scattering measurement [7]. Note, however, that their threshold values (filled blue triangles in Fig. 1.5a) were much higher than the values obtained by Siems et al. The monotonous decrease observed is intuitively understandable because the particle cooling depends on the surface-to-volume ratio and cooling is faster for smaller diameters [23]. Indeed, with the rigorous computational method using a hydrodynamic model and thermal model, the Marebia group obtained a monotonous decrease curve [10]. Their hydrodynamic model used in-depth treatment of bubble generation in terms of density change of water. The previous thermal model calculated spaciotemporal distribution of temperatures in the medium surrounding a Au NP [24]. By contrast to the result of Merabia,

numerical calculations using the thermal model by Baffou shown in Fig. 1.5c have displayed that the dependence of the fluence threshold with respect to the nanoparticle diameter features a bathtub profile [18], with a minimum fluence threshold at around 60 nm in diameter, in good agreement with the experimental observation by the Hashimoto group given in Fig. 1.5b. The points of discussion by Baffou are as in the following.

(i) The threshold fluence increase for small NPs is due to fast energy release to the surroundings.
(ii) The threshold fluence increase for large NPs arises from the nonlinear absorption cross section with respect to the NP volume. For small diameters below 60 nm, the absorption cross section is proportional to the NP volume but saturates.
(iii) Under fs-pulsed illumination, and under the assumption of no interface thermal resistivity, the maximum temperature increase δT_{NP} can simply be calculated using $\delta T_{NP} = \sigma_{abs} F / V c_m$ (σ_{abs}: absorption cross section of the NP, F: fluence of the pulse, V: NP volume and c_m: volumetric heat capacity of gold), without conducting numerical simulations, except for NP diameters smaller than 40 nm.
(iv) A NP interface thermal resistivity has no effect under ns-pulsed illumination, except for large NPs and large values of the interface thermal resistivity.
(v) A NP interface thermal resistivity has a strong effect in the fs-pulsed regime, irrespective of the nanoparticle diameter.

With respect the curve shape, computational curve by the Merabia group and that by the Baffou group is somewhat contradictory. Although the Merabia group was aware of the previous result by Baffou et al., the former did not comment on this point. The Merabia's group were much concerned about the difference of their computational result from the experimental threshold values. They argued that the threshold values by hydrodynamic calculation may have remarkable improvement if they consider the melting Au NPs during the bubble formation (Fig. 1.5d). With bubble generation, melting and evaporation of Au NPs have been postulated previously since the particle temperatures can go somewhat uncontrollably high inside the bubble [24].

At this point, we highlight the issue that the single particle study gave at least an order of magnitude greater threshold fluences of colloidal experiment (Fig. 1.5a). To account for their greater values, the Lapotko group ascribed to the Laplace pressure, the effect of surface tension, on the threshold of a bubble generation by optical heating. The Laplace pressure is given by $P_{Laplace} = 2\gamma / R_{bubble}$ (γ: surface tension, R_{Bubble}: bubble radius) and acts to collapse a bubble to a greater extent as the radius is smaller. However, the calculation by the Merabia group revealed that the effect of the Laplace pressure is minor [10]. From the experimental point of view, we can point out that measuring an accurate fluence is challenging because of uncertainties in measuring beam diameters and intensities under the microscope.

Finally, we describe bubble lifetimes on pulsed-laser excitation. Ensemble studies on 100 fs excitation of bubble dynamics using time-resolved X-ray measurements revealed that the lifetime of a bubble surrounding a 9-nm-diameter Au NP was

400 ps (max. bubble diameter: 20 nm) at 40 mJ cm^{-2}, and the lifetime of a bubble surrounding a 36-nm-diameter Au NP was 1.7 ns (max. bubble diameter: 75 nm) at 13.8 mJ cm^{-2} that is a threshold fluence [3, 4]. The bubble dynamics were well modeled using the Rayleigh–Plesset equation [25]. The Hashimoto group observed the bubble lifetime of 10 ns for 60-nm-diameter colloidal Au NPs irradiated with 15 ps lasers at a wavelength of 355 nm and a fluence f 5.2 mJ cm^{-2} (threshold fluence), using a transient extinction spectroscopy [8]. The maximum diameter observed was 260 ± 40 nm. In this case, the bubble decay time was much longer than the rise time, which is inconsistent with the Rayleigh–Plesset equation. The Lapotko group measured the bubble lifetime by observing the optical scattering response of a single Au NP that was excited by a 532 nm laser with a pulse width of 0.5 ns. They obtained bubble lifetimes of 18 ± 3.5 ns for a 30-nm-diameter Au NP and 9 ± 1 ns for single 90 and 250-nm-diameter Au NPs [7, 12]. They found that the lifetime of NP-generated bubbles increased with increasing incident fluence and that the vapor bubble lifetime was proportional to the maximum bubble diameter. Although the proportionality of bubble lifetime and maximum diameter is a rule of sum that well-describes the plasmonic nanobubbles, systematic studies are still lacking to describe precisely the pulse width-, fluence- and particle size-dependent lifetimes.

1.3 Recent Applications

The vapor nanobubbles photothermally generated using Au NPs have been demonstrated for potential applications in cancer therapy using bubble-induced shock waves [26], photoacoustic imaging using photoacoustic signals from bubbles [27] or solar energy conversion exploiting photothermal boiling of water [28]. These areas are still in progress to produce meaningful outcomes. Of particular interest is the solar bubble generation that has a potential application to sterilizing water in developing countries [29]. Recently, we have seen unprecedented applications of pulsed-laser-induced plasmonic bubbles in various fields. Here overview a few examples.

1.3.1 High-Speed Movement of Au NPs Encapsulated in a Nanoscale Bubble

Light can move objects through optical forces, enabling optical delivery of microparticles and NPs [30]. The optical manipulation is applicable to optical sorting, i.e., separation of particles exploiting particle size and material properties such as a refractive index. Previously, it was not feasible to give control over the velocities of moving particles. The achieved moving speed was 10–100 $\mu m\ s^{-1}$ so far [31, 32]. Here, we show an example of bubble-induced high-speed motions realized by irradiating femtosecond laser pulses at a high repetition rate.

512121_1_En_1_Chapter ☑ TYPESET ☐ DISK ☐ LE ☑ CP Disp.:27/12/2021 Pages: 20 Layout: T1-Standard

In this case, directed motions of silica-core Au-shell NPs (100-nm-diameter silica-core 10-nm-thick Au shell) suspended in water were activated by irradiating a 800 nm (center wavelength) laser beam with a repetition rate of 80.7 MHz (the pulsed duration is 94 fs, and the time interval between pulses is 12.4 ns) [33]. The fs laser was focused by passing through a 20 × objective lens (numerical aperture: 0.4). The power of 690 mW exceeded the bubble formation threshold, and the bubble encapsulated the NPs. As a result, some NPs were found to move along the beam propagation direction (positive motion), and some in the opposite direction (negative motion). Au NPs moved with unprecedented speeds both for the positive (maximum speed: 336,000 $\mu m\ s^{-1}$) and for the negative (maximum speed: 245,000 $\mu m\ s^{-1}$) directions. The forward and backward movements were produced by not only optical pushing but also pulling forces from a single Gaussian beam. Optical forces that may act on the NP can depend on the location relative to the laser focus as illustrated in Fig. 1.6. The two major forces are gradient force (G) and scattering force (S). The gradient force, G heads to the laser focus where the magnitude of G is zero because it depends on the intensity gradient. On the contrary, S is always in the direction of beam propagation, and its magnitude is proportional to the laser intensity. It is reasonable to assume that the optical force at the initial position determines the particle movement.

The enormously high speeds observed were interpreted as the following: While the laser-excited NP encapsulated in a bubble moves forward, it keeps evaporating water, maintaining a vapor cushion in front of it, and extends the bubble boundary forward.

Although not described in the study above, we suspect a potential effect of laser-induced evaporation that can accelerate the Au NPs. Without a continuous boosting mechanism, it seems difficult to maintain such a high speed that was originally realized by initial optical forces. As already mentioned, Au NPs can melt and evaporate inside the bubble [24] because of high-intensity laser heating. It has been demonstrated that ~40 μm-sized spherical stainless particles were accelerated in air caused by an evaporative propulsion force in the direction of laser beam propagation when irradiated with a 1070 nm CW laser with an output of 1–2 MW cm^{-2} [34]. In this case, an approximate speed of 12,500,000 $\mu m\ s^{-1}$ was achieved. Additionally, it

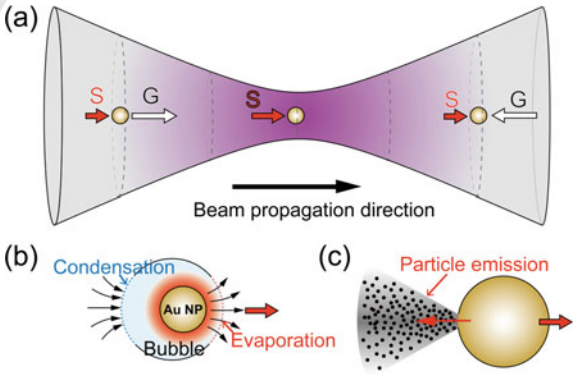

Fig. 1.6 **a** Optical forces acting on Au NPs along the laser beam propagation direction. S represents the scattering force, while G represents the gradient force. The direction and the magnitude of the forces are dependent on the location relative to the laser focus. **b** Bubble-induced propulsion. **c** Acceleration due to heating-induced emission of small particles

has been demonstrated that micrometer-sized platinum and other metal particles migrated inside melt borosilicate glass at a speed of 10,000 μm s^{-1} in the counter direction of the laser beam when illuminated by 514 nm CW laser at a power of 1 MW cm^{-2} [35]. These results suggest that evaporative propulsion can significantly accelerate the movement of particle under laser heating.

1.3.2 Micro- and Nano-Lasers Encapsulated in Bubble

Plasmonic bubbles have been applied to optical enhancer for laser oscillation at small scales. In one approach, photoexcitation of a single plasmonic NP in solution enabled a whispering-gallery-mode (WGM) droplet resonator associated with small micro/nanobubbles, formed by laser-induced heating [36]. Droplets containing dye-generated lasing modes with wavelengths depend on the size of the droplet, refractive index of the medium and surrounding environment. It was demonstrated that colloidal suspension of 20-nm-diameter Au NPs gave cavity diameters of 4.8 μm with a free spectral range (FSR) of 12 nm when excited with a 130 fs pulse with a central wavelength of 400 nm and at a repetition rate of 1 kHz (Fig. 1.7a). The droplets containing Coumarin 500 and plasmonic NPs showed sharp emission peaks in the wavelength range of 475–515 nm. WGM resonators are usually fabricated from solid-state materials. Soft cavities created with liquids or gels permit direct sensing where an optical cavity is both the sensing unit and the sample under analysis. In addition, soft cavities enable strong interactions of a plasmonic NP with the WGMs because of its location inside the cavity mode.

Another example is a solid-type laser named spaser (**s**urface **p**lasmon **a**mplification by **s**timulated **e**mission of **r**adiation). The spaser consists of a plasmonic NP surrounded by a nanoshell of the gain medium (Fig. 1.7b, left). The spaser can generate a single mode emission that is a spectrally tunable bright light

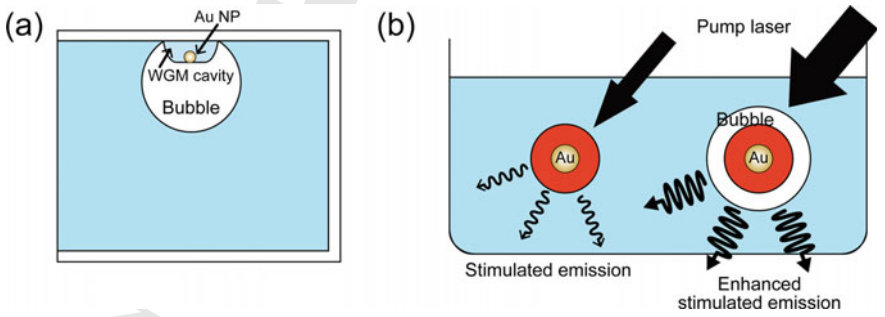

Fig. 1.7 Schematic of bubble-enhanced surface plasmon lasers; **a** single plasmonic NP in solution realizing a whispering-gallery-mode (WGM) droplet resonator associated with small micro/nanobubbles, **b** left: so-called spaser consisting of a Au NP core and a silica-shell embedded with laser dye molecules; right: a spaser encapsulated in a photothermal nanobubble

without saturation. The properties originate from stimulated emission amplification effects. Specifically, the plasmonic nanolaser was constructed by a core–shell structure consisting of a Au NP surrounded by a silica-shell doped with a uranine (disodium fluorescein) dye [37]. In this example, the excitation was provided by an OPO laser at a wavelength of 488 nm with 5–7 ns pulses. Using a 22 nm spaser with a 10 ± 1.9-nm-diameter Au NP core and a 6 ± 2.2 nm-thick shell, the lasing threshold was observed at a laser energy fluence of 26 ± 6.3 mJ cm^{-2}. For a lager 60 nm spaser, the threshold was reduced to 1.9 ± 0.6 mJ cm^{-2}. Above the threshold, the light output—pump in dependence demonstrated a straight line with emission spectral narrowing from 30–40 nm to 8–10 nm. Further increase in pump fluence led to the formation of vapor nanobubbles around spasers due to laser heating of the spaser particle leading to evaporation of the liquid medium surrounding the particle (Fig. 1.7b right). The appearance of bubbles is accompanied by nonlinear enhancement of stimulated emission intensity and further width narrowing. The maximum ratio of the stimulated emission intensity to the spontaneous emission background was 740 ± 95. The narrowest emission peak observed was 0.8 ± 0.2 nm. Both parameter levels were significant improvements over the previous results.

The origin of enhancement of spasing due to nanobubble formation has been ascribed to strong refractive, scattering and thermal lens effects in highly localized heated areas, especially in the associated bubbles that can be responsible for the light concentrating and redirecting. The original (without a nanobubble) spaser is a nanoshell with a Au core covered with dielectric shell containing dye molecules to produce the gain, embedded in water (the uniform medium). When a nanobubble is formed, another nanoshell appears between the gain shell and the embedding medium that contains water vapor. According to the authors, the main effect of the formation of a vapor nanobubble around the spaser is that dielectric screening of the surface plasmon-induced charge is reduced. This leads to an increase in the surface plasmon frequency, ω_n. In fact, the spaser frequency increases from the initial value of $\omega_n = 2.5$ eV in the absence of the nanobubble to $\omega_n = 2.6$ eV for a 30 nm radius nanobubble. If the gain medium working frequency, ω_n, exceeds the plasmon frequency, then the nanobubble formation brings the spaser closer to a perfect resonant condition. Consequently, the stimulated radiation of the surface plasmons becomes more efficient, which has been shown by this article. Presumably, the nanobubbles can provide dynamic optical feedback from its "wall" boundary, as well as refraction effects that can also lead directional emission.

1.3.3 Plasmonic Nanobubble Can Disrupt Cell Membrane and Biofilm

There is a great interest in delivering macromolecular agents into living cells for therapeutic purpose. Physical methods including electroporation using electric pulses and sonoporation using ultrasounds have been developed but they still suffer from

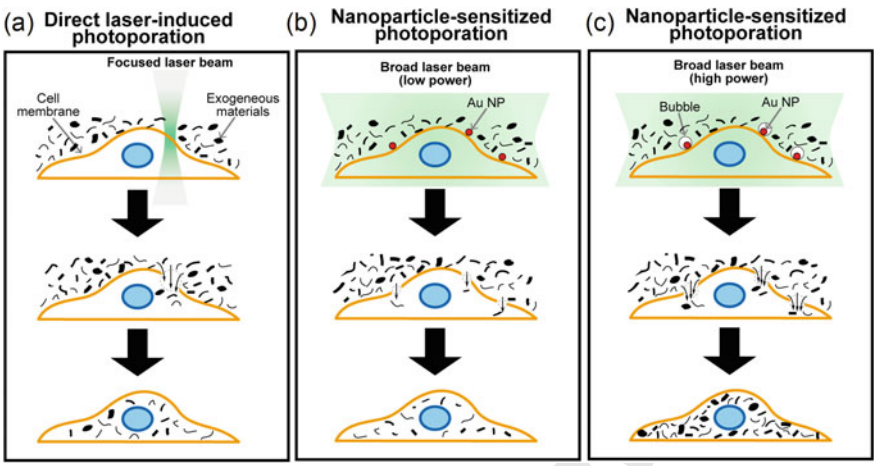

Fig. 1.8 Schematic overview of laser-induced photoporation on cell membrane, followed by the introduction of polymers into cells. **a** Direct laser-induced photoporation, **b** Au NP-assisted photoporation due to heating of the cell membrane at relatively small laser intensities, and **c** Au NP-assisted photoporation assisted by heating-induced bubble formation around the Au NPs

limited success in throughput and cell viability. Most importantly, translocation of the therapeutic macromolecules from the endosomes after endocytosis into the cytoplasm remains a major bottleneck. To overcome the difficulty, plasmonic nanobubble was used as a promising candidate for a physical approach to permeate the cell membrane [38].

First, Au NPs were adsorbed onto HeLa cells' surface from solution. Subsequently, positively charged Au NPs (70 nm) were used to facilitate interaction with the negatively charged cell membrane. Following the incubation of cells, Au NPs were adsorbed. A pulsed-laser irradiation was performed (pulse duration: 7 ns; wavelength: 561 nm from OPO laser). A low energy led to the heating of the cell membrane, while vapor nanobubbles were formed at high laser intensities above the threshold, 1.02 J cm^{-2}. The threshold observed is much higher than those observed previously in aqueous solution. Confocal microscopy images were acquired to test the viability of the cells labeled with calcein red-orange AM and the intracellular delivery of fluorescein isothiocyanate (FITC)-dextran (10 kDa). There was no noticeable decrease in cell viability up to 2.04 J cm^{-2}. Further increasing the laser fluence to 4.08 J cm^{-2} reduced the number of positive cells, likely due to the onset of cytotoxic effect of vapor nanobubbles that can damage cells when they grow large. FITC-dextran loading was much more efficient when mediated by plasmonic nanobubbles than by direct heating of the plasma membrane. For instance, the loading efficiency of 10 kDa FITC-dextran increased 2.5 fold by heating at 0.38 J cm^{-2} from the control, whereas it increased 12.5 fold of control by irradiation at nanobubble-forming 4.08 J cm^{-2}.

The conceptual scheme of photoporation on cell membrane to introduce polymers into cells is shown in Fig. 1.8. In this scheme, direct laser-induced photoporation without Au NPs (a), Au NP-assisted photoporation due to heating of the cell membrane (b) and Au NP-assisted photoporation assisted by laser-induced bubble formation around the Au NPs (c) is compared. The direct photoporation (a) can cause damages or kill the cells because of focused laser illumination, whereas the focused illumination can be avoided in the presence of Au NPs (b, c) because of efficient heat generation local to the membranes even with low intensities. There is little damage to the cells because of unfocused illumination. In (b), the resultant pores are small in sizes, and the number of pores is small because of weak intensities. By contrast, in (c), both the sizes of pore diameters and the numbers of pores will be increased compared with (b). As a result, more polymers can be incorporated into the cells. Still, the cell viability is maintained up to at a certain laser intensity.

The other application is to destroy biofilms exploiting plasmonic nanobubbles [39]. Biofilm forms when bacteria adhere to surfaces in moist environments by excreting a slimy, glue-like substance. Sites for biofilm formation include all kinds of surfaces. The biofilms serve to the decreased sensitivity of bacteria toward antibiotics. Thus, it is important to disturb biofilm integrity to improve antibiotics diffusion. The experimental result has shown that bacteria were loaded with cationic 70 nm Au NPs and that subsequent laser illumination of 7 ns pulses at 561 nm (fluence: 1.69 J cm^{-2}) resulted in plasmonic bubble formation inside the biofilms. Such nanobubble formation has led to substantial biofilm disruption, increasing antibiotic tobramycin efficacy up to 1–3 orders of magnitude. Enhancing antibiotic penetration through biofilm via laser-induced plasmonic nanobubble is a promising rout to solve the problem of biofilm-related infections.

1.4 Summary and Future Outlook

This chapter overviewed pulsed-laser-induced explosive bubble formation from solvent next to plasmonic Au NPs. The mechanism is regarded as purely photothermal boiling and not ascribable to cavitation, when the excitation wavelengths corresponding to the LSPR of Au NPs are employed. Although fundamental physics behind the transient plasmonic bubbles has been revealed in every detail using rigorous simulations [9, 10], still both experimental and computational efforts are needed to precisely characterize threshold fluences and state of materials inside the bubbles. For instance, experimental improvement such as single particle/single shot measurement is needed to avoid ensemble averaging effect. The dynamics governing particle melting/evaporation during bubble formation has not been fully characterized theoretically. We should point out that bubble generation using pulsed lasers has its own merit over CW laser-induced bubble generation. Since pulsed lasers have the advantage of outputting a high peak power within a limited pulse duration, they can provide means to obtain high spaciotemporal control for bubbles [39]. On the contrary, CW laser excitation results in severe medium heating for long period

of time, which results in collective medium heating [13]. Such a heating can be harmful to biological systems. As future prospects, the transient plasmonic nanobubbles can contribute to chemistry as photothermal nanoreactors for promising use. In the past, we saw the enhanced photothermal evaporation and size reduction of Au NPs inside the bubbles [24]. We expect that catalytic reactions of molecules concentrated on the outer surface of Au NPs can proceed triggered by bubble generation. Most importantly, the chemical reactions can be confined only at Au surfaces in a steam environment, while outer liquid space is kept at room temperature. Thus, we may see an impressive development of various nanochemisry in such an unconventional environment in the years to come.

References

1. U. Kreibig, M. Vollmer, *Optical Properties of Metal Clusters* (Springer, Berlin, 1995). https://doi.org/10.1007/978-3-662-09109-8
2. M.L. Brongersma, N.J. Halas, P. Nordlander, Plasmon-induced hot carrier science and technology. Nat. Nanotech. **10**, 25−34 (2015). https://www.nature.com/articles/nnano.2014.311
3. V. Kotaidis, A. Plech, Cavitation dynamics on the nanoscale. Appl. Phys. Lett. **87**, 213102. (2005). https://doi.org/10.1063/1.2132086
4. V. Kotaidis, C. Dahmen, G. von Plessen, F. Springer, A. Plech, Excitation of nanoscale vapor bubbles at the surface of gold nanoparticles in water. J. Chem. Phys. **124**(2006). https://doi.org/10.1063/1.2187476
5. M. Hu, H. Petrova, G.V. Hartland, Investigation of the properties of gold nanoparticles in aqueous solution at extremely high lattice temperatures. Chem. Phys. Lett. **391**, 220–225 (2004). https://doi.org/10.1016/j.cplett.2004.05.016
6. A. Siems, S.A.L. Weber, J. Boneberg, A. Plech, Thermodynamics of nanosecond nanobubble formation at laser-excited metal nanoparticles. New J. Phys. **13**, 043018 (2011). https://doi.org/10.1088/1367-2630/13/4/043018
7. E. Lukianova-Hleb, L.Y. Hu, L. Latterini, L. Tarpani, S. Lee, R.A. Drezek, J.H. Hafner, D.O. Lapotko, Plasmonic nanobubbles as transient vapor nanobubbles generated around plasmonic nanoparticles. ACS Nano **4**, 2109 (2010). https://doi.org/10.1021/nn1000222
8. T. Katayama, K. Setoura, D. Werner, H. Miyasaka, S. Hashimoto, Picosecond-to-nanosecond dynamics of plasmonic nanobubbles from pump–probe spectral measurements of aqueous colloidal gold nanoparticles. Langmuir **30**, 9504−9513 (2014) https://pubs.acs.org/doi/abs/https://doi.org/10.1021/la500663x.
9. K. Metwally, S. Mensah, G. Baffou, Fluence threshold for photothermal bubble generation using plasmonic nanoparticles. J. Phys. Chem. C **119**, 28586−28596 (2015). https://doi.org/10.1021/acs.jpcc.5b09903
10. J. Lombard, T. Biben, S. Merabia, Threshold for vapor nanobubble generation around plasmonic nanoparticles. J. Phys. Chem. C **121**(28), 15402–15415 (2017). https://doi.org/10.1021/acs.jpcc.7b01854
11. A. Vogel, S. Busch, U. Parlitz, Shock wave emission and cavitation bubble generation by picosecond and nanosecond optical breakdown in water. J. Acoust. Soc. Am. **100**, 148−165 (1996). https://doi.org/10.1121/1.415878
12. G. Baffou, J. Polleux, H. Rigneault, S. Monneret, Super-heating and micro-bubble generation around plasmonic nanoparticles under cw illumination. J. Phys. Chem. C **118**, 4890–4898 (2014). https://doi.org/10.1021/jp411519k

13. G. Baffou, *Thermoplasmonics Heating Metal Nanoparticles Using Light* (Cambridge University Press, Cambridge, England, 2017). https://doi.org/10.1017/9781108289801
14. C.P. Lin, M.W. Kelly, Cavitation and acoustic emission around laser-heated microparticles. Appl. Phys. Lett. **72**, 2800−2802 (1998). https://doi.org/10.1063/1.121462
15. A. Plech, V. Kotaidis, S. Gresillon, C. Dahmen, G. von Plessen, Laser-induced heating and melting of gold nanoparticles studied by time-resolved x-ray scattering. Phys. Rev. **B70**, 195423 (2004). https://doi.org/10.1103/PhysRevB.70.195423
16. E.Y. Lukianova-Hleb, D.O. Lapotko, Influence of transient environmental photothermal effects on optical scattering by gold nanoparticles. Nano. Lett. **9**, 2160−2166 (2009). https://doi.org/10.1021/nl9007425
17. C. Burda, X. Chen, X.R. Narayanan, R.M.A. El-Sayed, Chemistry and properties of nanocrystals of different shapes. Chem. Rev. **105**, 1025–1102 (2005). https://doi.org/10.1021/cr030063a
18. X. Fu, B. Chen, J. Tang, A.H. Zewail, Photoinduced nanobubble-driven superfast diffusion of nanoparticles imaged by 4D electron microscopy. Sci. Adv. **3**, e1701160 (2017). https://advances.sciencemag.org/content/3/8/e1701160
19. E. Acosta, M.G. Gonz´alez, P.A. Sorichetti, G.D. Santiago, Laser-induced bubble generation on a gold nanoparticle: A nonsymmetrical description. Phys. Rev. E **92**, 062301 (2015). https://doi.org/10.1103/PhysRevE.92.062301
20. S. aus der Wiesche, C. Rembe, E.P. Hofer, Boiling of superheated liquids near the spinodal: I General theory. Heat Mass Transf. **35**, 25−31 (1999). https://doi.org/10.1007/s002310050294
21. A. Vogel, V. Venugopalan, Mechanisms of pulsed laser ablation of biological tissues. Chem. Rev. **103**, 577–644 (2003). https://doi.org/10.1021/cr010379n
22. Z. Liu, W.H. Hung, M. Aykol, D. Valley, S.B. Cronin, Optical manipulation of plasmonic nanoparticles, bubble formation and patterning of SERS aggregates. Nanotechnology **21**(2010). https://doi.org/10.1088/0957-4484/21/10/105304
23. M. Hu, G.V. Hartland, Heat dissipation for Au particles in aqueous solution: Relaxation time versus size. J. Phys. Chem. B **106**, 7029–7033 (2002). https://doi.org/10.1021/jp020581+
24. S. Hashimoto, D. Werner, T. Uwada, Studies on the interaction of pulsed lasers with plasmonic gold nanoparticles toward light manipulation, heat management, and nanofabrication. J. Photochem. Photobiol. C **13**, 28–54 (2012). https://doi.org/10.1016/j.jphotochemrev.2012.01.001
25. M.S. Plesset, M. Prosperetti, Bubble dynamics and cavitation. Ann. Rev. Fluid Mech. **9**, 145–185 (1977). https://doi.org/10.1146/annurev.fl.09.010177.001045
26. D. Lapotko, Plasmonic nanobubbles as tunable cellular probes for cancer theranostics. Cancers **3**, 802–840 (2011). https://doi.org/10.3390/cancers3010802
27. T. Yin, P. Wang, R. Zheng et al., Nanobubbles for enhanced ultrasound imaging of tumors. Int. J. Nanomed. **7**, 895–904 (2012). https://doi.org/10.2147/IJN.S28830
28. O. Neumann, A.S. Urban, J. Day et al., Solar vapor generation enabled by nanoparticles. ACS Nano **7**, 42–49 (2013). https://doi.org/10.1021/nn304948h
29. Solar water sterilization enabled by photothermal nanomaterials, Nano Energy **87**(2021). https://doi.org/10.1016/j.nanoen.2021.106158
30. P. Zemanker, G. Volpe, A. Jonas et al., Perspective on light-induced transport of particles: From optical forces to phoretic motion. Adv. Opt. Photon. **11**, 577–678 (2019). https://doi.org/10.1364/AOP.11.000577
31. A. Königer, W. Köhler, Optical Funneling and trapping of gold colloids in convergent laser beams. ACS Nano **6**, 4400–4409 (2012). https://doi.org/10.1021/nn301080a
32. V. Kajorndejnukul, W. Ding, S. Sukhov et al., Linear momentum increase and negative optical forces at dielectric interface. Nature Photon. **7**, 787–790 (2013). https://www.nature.com/articles/nphoton.2013.192
33. E. Lee, D. Huang, T. Luo, Ballistic supercavitating nanoparticles driven by single Gaussian beam optical pushing and pulling forces. Nat. Commun. **11**, 2404 (2020). https://www.nature.com/articles/s41467-020-16267-9

34. T. Mitra, A.K. Brown, D.M. Bernot et al., Laser acceleration of absorbing particles. Opt. Express **26**, 6639–6652 (2018). https://doi.org/10.1364/OE.26.006639
35. Metal particle manipulation by laser irradiation in borosilicate glass. Opt. Express **18**, 20313–20320 (2010). https://doi.org/10.1364/OE.18.020313
36. R. Sato, J. Henzie, S. Ishii, K. Takazawa, Y. Takeda, Plasmonic-induced self-assembly of WGM cavities via laser cavitation. Opt. Express **28**, 31923–31931 (2020). https://doi.org/10.1364/OE.401662
37. E. Galanzha, R. Weingold, D. Nedosekin et al., Spaser as a biological probe. Nat. Commun. **8**, 15528 (2017). https://doi.org/10.1038/ncomms15528
38. R. Xiong, K. Raemdonck, K. Peynshaert et al., Comparison of gold nanoparticle mediated photoporation: Vapor nanobubbles outperform direct heating for delivering macromolecules in live cells. ACS Nano **8**, 6288–6296 (2014). https://doi.org/10.1021/nn5017742
39. E. Teirlinck, R. Xiong, T. Brans et al., Laser-induced vapour nanobubbles improve drug diffusion and efficiency in bacterial biofilms. Nat. Commun. **9**, 4518 (2018). https://www.nature.com/articles/s41467-018-06884-w
40. C.J. Trout, J.A. Clapp, J.C. Griepenburg, Plasmonic carriers responsive to pulsed laser irradiation: a review of mechanisms, design, and applications. New J. Chem. (2021). https://doi.org/10.1039/D1NJ02062E